



Article

Laser-Induced Copper/Carbon Nanocomposite from Anodically Electrodeposited Chitosan for H₂O₂ Sensing

Usama Zafar^{1,2}, Prince Kumar Rai³, Ankur Gupta³ , Jan G. Korvink¹ , Vlad Badilita^{1,*} and Monsur Islam^{1,*}

¹ Institute of Microstructure Technology, Karlsruhe Institute of Technology, Hermann-von-Helmholtz-Platz 1, 76344 Eggenstein-Leopoldshafen, Germany; usamazafar62paf@gmail.com (U.Z.); jan.korvink@kit.edu (J.G.K.)

² Institut für Mikrosystemtechnik (IMTEK), Universität Freiburg, Georges-Köhler-Allee 103, 79110 Freiburg im Breisgau, Germany

³ Department of Mechanical Engineering, Indian Institute of Technology Jodhpur, Jodhpur 342030, India; ankur Gupta@iitj.ac.in (A.G.)

* Correspondence: vlad.badilita@kit.edu (V.B.); monsurislam79@gmail.com (M.I.)

Abstract: This work presents anodically electrodeposited copper (Cu)/chitosan gel as a novel precursor for synthesizing a Cu/carbon nanocomposite through laser-induced carbonization. Metal/carbon nanocomposites offering advantageous properties compared to their individual counterparts stand out in various applications, particularly in those involving electrochemical phenomena. However, their synthesis often suffers from complicated and time-consuming synthesis procedures. Here, we integrate anodic electrodeposition and laser-induced carbonization to yield a rapid, simple, and inexpensive procedure for synthesizing metal/carbon nanocomposite. A precursor composite involving Cu-coordinated chitosan film is achieved through anodic electrodeposition on a copper anode. Irradiation by an infrared laser with optimized parameters results in the thermochemical decomposition of the Cu/chitosan composite, rapidly forming a nanocomposite material featuring highly graphitized and porous carbon materials. Elemental mapping confirms the formation of the nanocomposite, although no crystalline phases of copper are observed during X-ray diffraction. This can be attributed to the rapid nature of the laser-carbonization process. The nanocomposite material is further demonstrated for electrochemical sensing of hydrogen peroxide (H₂O₂), exhibiting a sensitivity of 2.65 mM⁻¹ for concentrations ranging from 0.01 mM to 0.1 mM H₂O₂, and 0.01 ± 0.01 mM⁻¹ for concentrations from 0.1 to 10 mM H₂O₂. These sensitivities are comparable to other non-enzymatic H₂O₂ biosensors. The finding of this work signifies a rapid and facile method for synthesizing metal/carbon nanocomposites with strong implications for the field of biosensors.

Keywords: chitosan; laser-induced graphene; electrodeposition; H₂O₂ sensor; biopolymer; nanocomposite



Citation: Zafar, U.; Rai, P.K.; Gupta, A.; Korvink, J.G.; Badilita, V.; Islam, M. Laser-Induced Copper/Carbon Nanocomposite from Anodically Electrodeposited Chitosan for H₂O₂ Sensing. *C* **2024**, *10*, 28. <https://doi.org/10.3390/c10020028>

Academic Editors: Stefano Bellucci and Gil Goncalves

Received: 31 January 2024

Revised: 14 March 2024

Accepted: 20 March 2024

Published: 24 March 2024



Copyright: © 2024 by the authors. Licensee MDPI, Basel, Switzerland. This article is an open access article distributed under the terms and conditions of the Creative Commons Attribution (CC BY) license (<https://creativecommons.org/licenses/by/4.0/>).

1. Introduction

Metal/carbon nanocomposites stand out as an interesting category of materials, exhibiting distinctive properties such as elevated electrical conductivity, exceptional wear resistance, and customizable electrochemical properties. These attributes have facilitated the widespread application of metal/carbon composites, particularly as electrode materials in sensor devices [1–5]. Specifically, in an electrochemical sensor device, where the carbon matrix provides a conductive and porous scaffold facilitating a high surface area, the embedded metal nanoparticles serve as the redox sites due to their electroactive properties. Typical methods for fabricating metal/carbon nanocomposites include metal deposition on a carbon material [6–8] and carbonization of a precursor composite material [9–12]. Typical deposition methods include sputtering and microwave plasma-enhanced chemical vapor deposition, which often require sophisticated and expensive infrastructure, rendering the process expensive and complex. Furthermore, deposition methods only result in

surface coating of carbon with metal, restricting the improvement of the bulk material. Conversely, the carbonization of a precursor composite offers a relatively simpler solution. However, the selection of compatible precursor materials for carbon and metal becomes a crucial factor, which often makes the precursor preparation more complex. As a potential solution to this, we recently introduced an anodically electrodeposited metal/chitosan hydrogel as a novel precursor for metal/carbon composite material [13]. Electrodeposition is a well-established electrochemical method employed for creating a coating on the conductive surface of an electrode [14–16]. Chitosan is one of the popular biopolymers studied for electrodeposition due to its unique chemical attributes [17,18]. Additionally, chitosan has also been popularly explored as a precursor to porous carbon materials for several applications [19–21]. Traditionally, cathodic electrodeposition is performed to create the coating of chitosan hydrogel, where chitosan particles dissolved in an acidic solution undergo a pH-sensitive cathodic neutralization mechanism during the electrodeposition process, resulting in the development of a transparent chitosan gel on the cathode surface. Our previous study showed that in a narrow pH range of 5–6, electrodeposition on the anode also occurred. However, contrasting to cathodic gels, the anodic gel appeared blue due to the incorporation of Cu^{2+} ions from the copper anode, making it a facile method for precursor preparation. Carbonization of the anodically electrodeposited copper/chitosan composite further resulted in a copper/carbon composite [13]. However, typical carbonization processes possess several disadvantages. The most popular carbonization process relies on a high-temperature furnace, within which a polymeric precursor is slowly (typical heating rate <10 °C/min) heated to a temperature greater than 700 °C in an inert atmosphere. Such a process is highly time-consuming and often requires expensive heating systems. Hydrothermal carbonization emerges as an alternative to oven-based pyrolysis [22,23]. However, hydrothermal systems are also complex and mostly result in powdered carbonaceous materials, losing the intrinsic precursor geometry. Both hydrothermal and oven-based carbonization yield the pyrolytic transformation of the bulk precursor material; design-controlled patterning is often extremely challenging in these conventional pyrolysis processes.

In recent years, laser-induced carbonization has emerged as a rapid and cost-effective method for readily and locally converting polymeric precursors into conducting carbon films utilizing localized laser irradiation [24–27]. This process is applicable across a broad spectrum of wavelengths. The laser-induced carbon (LIC) is formed through a combination of photochemical and photothermal mechanisms, resulting in the formation of highly porous, graphitized, carbon-rich films embedded directly in the polymer precursor. Unlike conventional carbonization processes, the laser-induced pyrolytic transformation can be achieved under ambient conditions, allowing for direct patterning of carbon without the need for a mask, utilizing a standard commercial laser engraving machine. While polyimide sheets are conventionally employed as the substrate for laser carbonization, several alternative polymers, including biopolymers, high-temperature thermoplastics, and thermosets, have been explored for the production of LIC materials [28–30]. LIC has proven to be a suitable method for producing chemical and biological sensors, leveraging the high surface activity [31–34]. These advantages enable precise detection at low concentrations of biological metabolites, such as urea [35], dopamine [36], H_2O_2 [37,38], thrombin [39], and glucose [29,40].

In this study, we integrate anodic electrodeposition of chitosan and laser-induced carbonization of the electrodeposited film for achieving a fast and facile method for producing metal/carbon nanocomposite material. We focus on Cu/carbon nanocomposite here, due to the popular choice of copper anode in electrodeposition, and the ability to readily form copper–chitosan coordination bonds [41,42]. We optimize the laser scribing conditions to facilitate laser carbonization. Furthermore, a detailed elemental and material characterization is performed to confirm the final composition of the laser-induced carbon/copper (Cu/LIC) nanocomposite material. Copper nanoparticles have been investigated by many researchers for the detection of H_2O_2 due to the capability of Cu nanoparticles in H_2O_2 activation and

reduction [43–45]. Utilizing this characteristic, we further investigate the electrocatalytic performance of the Cu/LIC material in the detection of H_2O_2 , to demonstrate its utility as an effective sensor material. This work underscores the utilization of electrodeposited composite precursors for laser carbonization in developing novel biosensors.

2. Experimental

2.1. Copper/Carbon Nanocomposite Electrode Fabrication

The electrodeposition of the chitosan hydrogel was performed using a chitosan poly-electrolyte. For a 120 mL chitosan solution, 1.2 g chitosan powder (Sigma Aldrich, St. Louis, MO, USA) product ID 448877–Deacetylation degree 75% to 85%, medium molecular weight) was dispersed in 115.2 mL of distilled water, to yield a chitosan concentration of 1% *w/v*, followed by adding 4% *v/v* 2 M hydrochloric acid (4.8 mL) into the solution with continuous stirring on a magnetic stirrer plate. As anodic electrodeposition occurs within a narrow pH range of 5–6, as reported in our previous publication [13], the pH of the solution was adjusted to 5.5 by adding 6 mL sodium hydroxide dropwise to the chitosan solution. During electrodeposition, copper foils were used both as cathode and anode. The electrodeposition process utilized a DC power supply (Votcraft VLP-1602 pro), and the output current was monitored using an HM 8112-3 Multimeter (Rohde & Schwarz GmbH & Co. KG, München, Germany). Chitosan electrodeposition was carried out at a DC voltage of 25 V applied to electrodes with a surface area of 100 mm^2 for a duration of 15 min. Electrodeposition of chitosan occurred on both electrodes, with the cathodic gel appearing white and the anodic gel exhibiting a distinct blue hue, as shown in Figure 1, attributed to the presence of Cu^{2+} ions within the chitosan matrix [13].

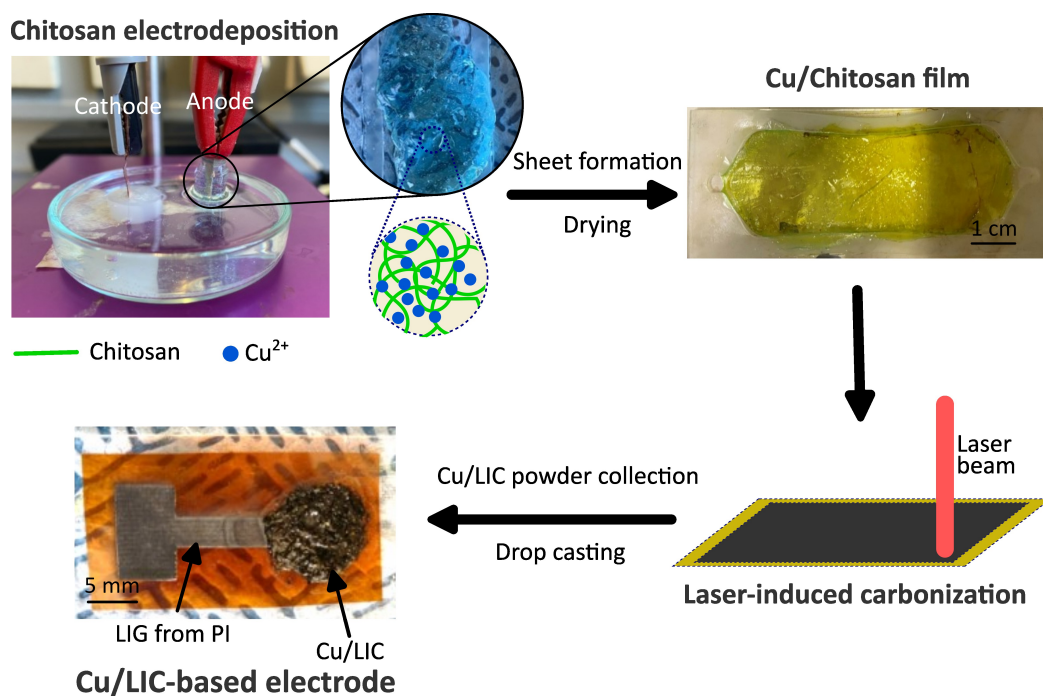


Figure 1. Schematic illustration of the fabrication of the laser-induced copper carbon (Cu/LIC)-based sensor electrode. The fabrication features laser-induced carbonization of anodically deposited Cu/chitosan hydrogel film. The Cu/LIC was further collected from the chitosan substrate and drop-casted using a binder on a laser-induced graphene (LIG) surface on a flexible polyimide (PI) sheet.

For laser carbonization, a flat substrate is typically required. To prepare a flat substrate, the anodically electrodeposited chitosan gel was meticulously scraped off from the anode surface and directly placed into an elastomer mold, followed by pressing between two glass slides and a 15 min treatment with acetone to minimize dehydration-assisted shrinkage.

The hydrogel was further dried at 90 °C for 1 h, resulting in a uniformly dried xerogel sheet used for the laser-induced carbonization. The carbonization process was performed by irradiation using a CO₂ laser beam (wavelength $\lambda = 10.6 \mu\text{m}$) in the engraving mode of a commercial laser cutting machine (ULS Versa Laser 3.50, Universal Laser Systems GmbH, Vienna, Austria). The speed of the laser scribing was kept constant at 15.6 cm/s, whereas the beam's power was varied from 1 W to 10 W with incremental increase to find the optimum carbonization condition. The laser beam was further defocused to 3 mm to enable the carbonization. As the carbonized film was not mechanically stable, it was not possible to use the laser-carbonized chitosan as free-standing electrodes. Therefore, we chose to use the carbonized material in powder form. To prepare a supporting electrode, we fabricated laser-induced graphene (LIG) electrodes by laser irradiation on flexible polyimide (PI) sheets. The process of fabricating PI-derived LIG material is detailed in our previous publications [27,46]. The Cu/LIC material obtained from the Cu²⁺/chitosan precursor was scratched from the precursor substrate and dispersed in a Nafion D520 binder solution. The Cu/LIC/Nafion dispersion was dropcasted on the LIG electrode to prepare the sensor electrode. The entire fabrication process is illustrated in Figure 1, including a digital photograph of our sensor electrode.

2.2. Characterization

The morphology of the composite laser carbon material was characterized using a field emission scanning electron microscope (SEM; SUPRA 60VP, Carl Zeiss AG, Oberkochen, Germany), and the elemental analysis was performed using the same scanning electron microscope equipped with an X-ray energy dispersive system (EDS, Oxford instruments GmbH, Wiesbaden, Germany). The composition and crystallinity of the materials studied here were investigated using X-ray diffraction (XRD) on a Bruker D8 Advance diffractometer (Bruker, Karlsruhe, Germany). The measurements used Cu-K $\alpha_{1,2}$ radiation ($\lambda = 1.5405 \text{ \AA}$). The Raman spectrum for the Cu/LIC material was acquired utilizing a Bruker Senterra instrument, which was outfitted with a DPSS laser (wavelength = 532 nm) operating at a laser power of 2 mW, ensuring a penetration depth of less than 1 μm . We further deconvoluted the Raman spectra using Gauss curve fitting using Origin 2021 software (OriginLab Corporation, Northampton, MA, USA) for the areal analysis of the peaks. The crystallite size (L_a) of the carbon material was estimated using the Tuinstra and Koenig equation, as proposed by Caçado et al. [47], which correlates L_a with the laser wavelength (λ) and integrated area ratio (A_D/A_G) of D-band and G-band, as shown in Equation (1):

$$L_a = \left(2.4 \times 10^{-10}\right) \lambda^4 \left(\frac{A_D}{A_G}\right)^{-1} \quad (1)$$

Transmission electron micrographs (TEM) were captured utilizing a Talos F200X G2 (Thermo Fisher Scientific, Dreieich, Germany), a high-resolution transmission and scanning electron microscope from Thermo Fisher Scientific in Germany, operating both in scanning transmission electron microscopy (STEM) and high-resolution TEM (HRTEM) mode. The elemental mapping of the Cu/LIC material was further performed by STEM-EDX using an FEI Super-X EDX system equipped with four SDDs (Silicon Drift Detectors) (Thermo Fisher Scientific, Dreieich, Germany).

2.3. H₂O₂ Sensing

The electrochemical sensing of hydrogen peroxide (H₂O₂) using Cu/LIC electrodes was performed in a standard three-electrode electrochemical setup using an Autolab PGSTAT302F electrochemical workstation (Metrohm AG, Herisau, Switzerland). The three-electrode system included Ag/AgCl saturated with KCl solution as the reference electrode, a platinum sheet as a counter electrode, and Cu/LIC deposited on the LIG substrate as the working electrodes. To perform the electrochemical tests, a 0.02 M phosphate-buffered saline (PBS) solution was used as the electrolyte. In this context, PBS served as a stable and pH-controlled environment for electrochemical reactions. Cyclic voltammetry (CV) was

performed for the electrodes with and without H₂O₂ to characterize the sensing behavior. The response of the Cu/LIC electrode to H₂O₂ was calculated by the ratio of the current response without and with the presence of H₂O₂. The sensitivity of the electrode material was further estimated by the slope of the linear curve fitting to the response with respect to the change in the H₂O₂ concentration. We calculated the limit of detection (LOD) using Equation (2), which correlates the standard deviation in the y-intercept (σ) in the linear curve fitting to the sensitivity (S):

$$LOD = \frac{3.3\sigma}{S} \quad (2)$$

3. Results and Discussion

We varied the power of the laser beam to find out the optimum laser parameters for laser carbonizing the Cu/chitosan xerogel film. The carbonization occurred within a very narrow power range. As shown in Figure 2a, no carbonization happened at a laser power of 1.2 W, whereas a power of 1.35 W resulted in good carbonization (Figure 2b). Even with a small increment in power, the laser started ablating the chitosan film, as illustrated in Figure 2c for a power of 1.5 W. This could be attributed to the film's thickness and the precursor's polysaccharide nature, as also seen in the case of other polysaccharide bipolymers [28,48]. Typically, polysaccharide precursors feature a low flash point, leading to easy ablation under laser treatment. Therefore, they need to be chemically or physically modified to enable laser carbonization. We assume chitosan also exhibited similar behavior. However, the copper ions in our composite xerogel might have helped the heat dissipation during the laser treatment, enabling the carbonization, even though the carbonization window was narrow. On the other hand, the low thickness (below 100 μm) of the film could make the carbonized film mechanically unstable, which prevented the fabrication of a free-standing electrode.

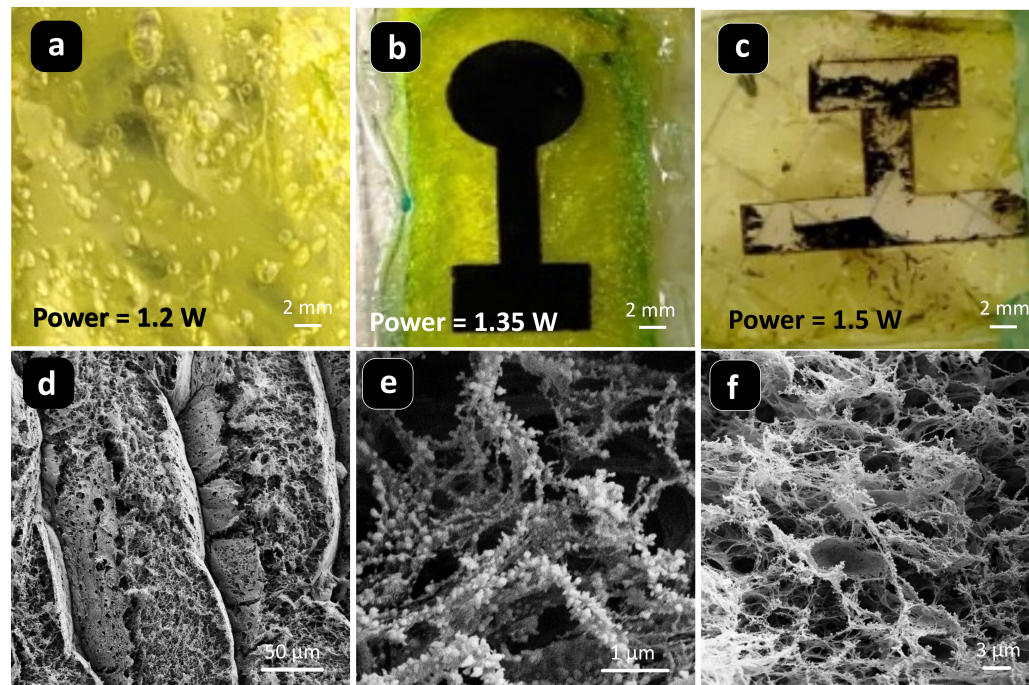


Figure 2. Cu/chitosan xerogel film treated with different laser powers, i.e., (a) 1.2 W, (b) 1.35 W, and (c) 1.5 W, illustrating the effect of laser power in laser carbonization of the chitosan film. (d–f) SEM images of the laser-carbonized Cu/chitosan film obtained for the laser power of 1.35 W, depicting the morphology of the obtained Cu/LIC material.

The microstructure of the Cu/LIC materials was examined through scanning electron microscopy (SEM). The trenches of the laser passes could be observed in Cu/LIC (Figure 2d),

which is often observed in laser-induced carbon materials [31,49,50]. Furthermore, the laser treatment resulted in a highly porous and fibrous morphology, as presented in Figure 2e,f. The irregular and random distribution of pore sizes and fibrous nature was attributed to the instantaneous photo-thermochemical decomposition of the precursor material under the rapid interaction with the laser pulses. Such morphological characteristics translate to a high surface area of the carbonized material. The SEM analysis further revealed that the fibrous network of Cu/LIC material was decorated with nanometric particles, as shown in Figure 2b.

To further characterize the composition of the Cu/LIC material, we performed Energy Dispersive X-ray (EDX) mapping in STEM. The results are presented in Figure 3. The EDX mapping confirmed the uniform distribution of carbon and copper. However, it also revealed a significant presence of sodium (Na), chlorine (Cl), and oxygen (O). As the laser carbonization was performed in ambient conditions, the formed carbon seemed to interact with the ambient oxygen, forming several oxygen-containing surface groups [35,46]. The copper present in the matrix could also interact with the ambient oxygen. Furthermore, chitosan itself is an oxygen-rich polymer, which could be attributed to the presence of oxygen. Figure 3d,e suggests that the Na and Cl were present in the sample in spherical sodium chloride (NaCl) particle form with a particle size around 100 nm. The distribution and shape of these particles resembled the particles decorating the fibrous network of Cu/LIC materials, as observed in Figure 2e. The presence of NaCl was further confirmed by XRD diffractogram (Figure 4a), which featured distinctive peaks at $2\theta = 27.25^\circ, 45.15^\circ, 53.76^\circ, 56.41^\circ, 66.18^\circ, \text{ and } 75.23^\circ$, corresponding to (111), (200), (220), (311), (222), (400), and (420) reflections of NaCl crystal (International Centre for Diffraction Data (ICDD) card number 78-0751 [51]). The presence of NaCl was also observed in the diffractogram of the precursor Cu/chitosan xerogel, suggesting the formation of NaCl during the electrodeposition step. For facilitating anodic electrodeposition, NaOH and HCl were utilized for pH adjustment and chitosan dissolution, respectively, which might have reacted to form NaCl within the polyelectrolyte. The formed NaCl was further encapsulated within the anodic gel matrix, persisting in the Cu/C composite post-carbonization. A similar phenomenon was also observed in our previous study on anodic electrodeposition of chitosan [13].

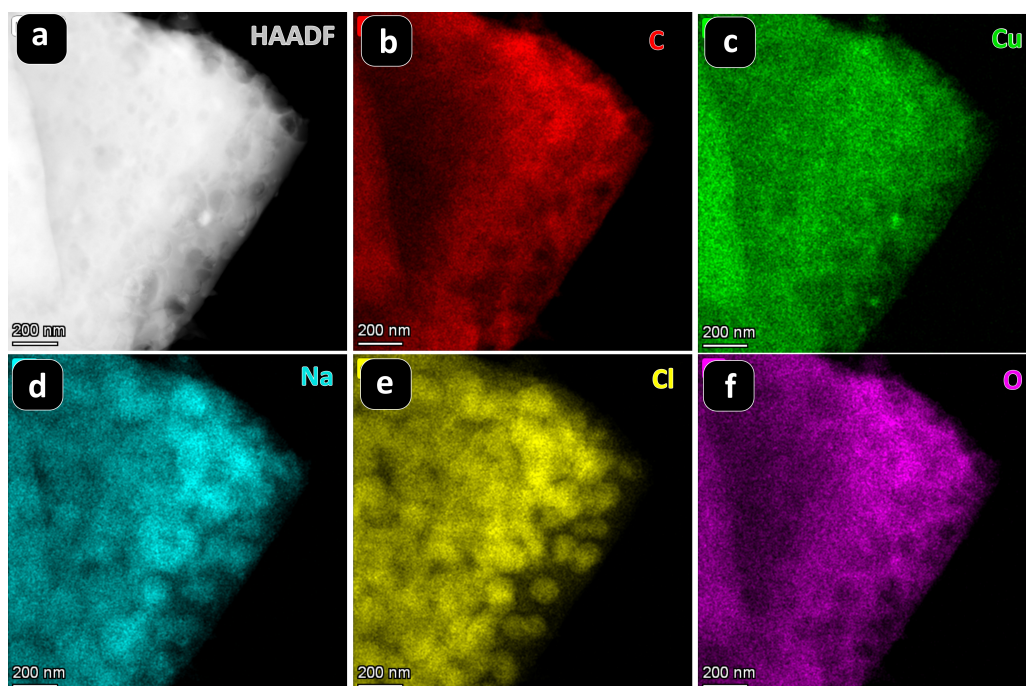


Figure 3. STEM characterization of Cu/LIC material. (a) High-angle annular dark-field (HAADF) image of the Cu/LIC material. EDX mapping of the corresponding sample confirms the presence of (b) carbon, (c) copper, (d) sodium, (e) chlorine, and (f) oxygen.

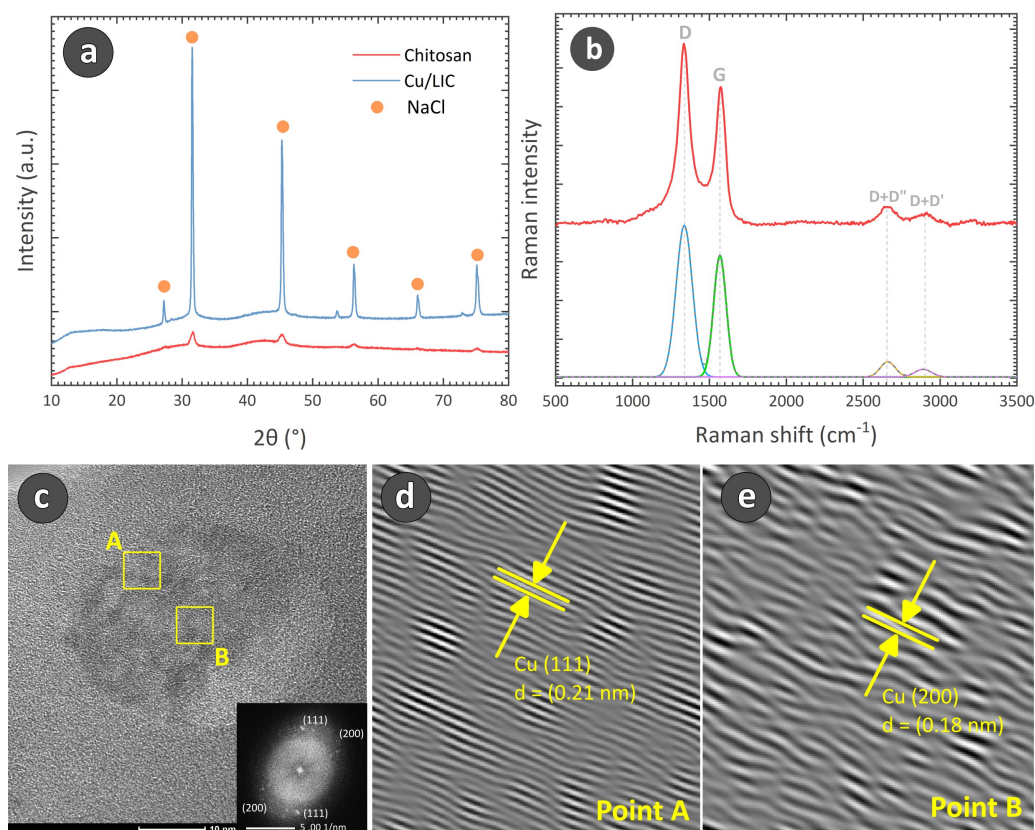


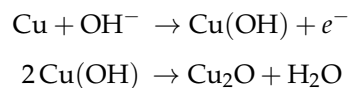
Figure 4. (a) XRD of anodically deposited chitosan and the Cu/LIC material derived from it through laser carbonization. (b) Raman spectra of Cu/LIC obtained from the laser carbonization of anodically electrodeposited chitosan and its deconvolution using Gaussian curve fitting. (c) HRTEM image of a copper nanoparticle found in the Cu/LIC material, and its corresponding FFT in the inset. (d,e) Lattice fringes of the selected areas in (c) showing the interlayer spacing of the selected copper crystallite.

However, to our surprise, no presence of copper was observed in the XRD diffractogram, even though EDX confirmed the uniform distribution of copper within the carbonized sample. As XRD peaks indicate the presence of crystalline phases of a material, the XRD diffractogram obtained here suggests that Cu/LIC did not feature any copper crystallites. In the electrodeposited gel, copper mainly coordinates with chitosan molecules, retaining its Cu^{2+} ionic form. As laser carbonization is a spontaneous phenomenon, it might not allow enough time for the sintering of the copper ions present in the xerogel, preventing the formation of crystallites. It suggests two possibilities: either copper still remained in the Cu^{2+} ionic form coordinating with the carbon network, or laser carbonization resulted in an amorphous copper matrix. However, a few crystallites of copper featuring a dimension of 10 nm to 30 nm could be observed during the TEM analysis. An example is presented in Figure 4c. The HRTEM images of the selected sections in Figure 4c further revealed the lattice fringes related to the copper crystal plane (111) and (200) in Figure 4d,e, respectively. The fast Fourier transform (FFT), as shown in the inset of Figure 4c, also confirmed the crystalline nature of the particle, depicting the diffraction of the (111) and (002) planes of Cu, further suggesting a face-centered cubic (fcc) structure (space group: Fm-3m) [52,53]. The occurrence of these crystallites was very infrequent within the Cu/LIC material, and they could not be detected in XRD. However, a further extensive characterization might be needed to understand the behavior of Cu/chitosan precursor under laser irradiation, which may confirm the ionic or amorphous state of the Cu within the resulting composite material.

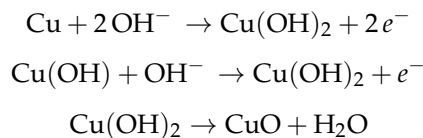
Raman spectroscopy was performed to characterize the nature of the laser-carbonized material. The Raman spectrum of Cu/LIC, as presented in Figure 4b, featured characteristic peaks at 1365 cm^{-1} and 1580 cm^{-1} , corresponding to the D and G peaks, respectively,

a typical characteristic of carbon-based materials [54,55]. The Cu/LIC material featured a peak intensity ratio (I_D/I_G) of 1.3, suggesting the presence of a significant amount of amorphous carbon. However, deconvolution of the spectra with Gaussian curve fitting revealed a low areal ratio (A_D/A_G) of 1.6, signifying a high graphitic nature of the carbon counterpart. Furthermore, the in-plane crystallite size, L_a for the carbon counterpart of Cu/LIC material was calculated to 11.9 nm, suggesting a turbostratic nature of the carbon material, with both graphitic and amorphous content [56,57]. The turbostratic nature of carbon could further be confirmed by the D+D'' and D+D' peaks around 2660 cm^{-1} and 2890 cm^{-1} , respectively, [58,59]. Notably, there was no detection of copper (I) oxide or copper (II) oxide peaks in the Raman spectrum, confirming no oxidation of the embedded copper during the laser carbonization process.

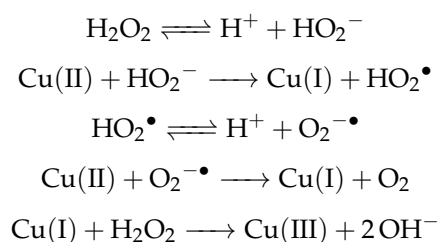
We investigated the electrochemical sensing capabilities of the Cu/LIC material for the detection of H_2O_2 . The cyclic voltammogram (CV) of the Cu/LIC electrode is presented in Figure 5a, which exhibited the specific cathodic and anodic peaks of copper in the presence of 1 mM H_2O_2 within the PBS electrolyte. During the potential sweep between -0.8 V to 0.6 V , two oxidative peaks were observed at 0.06 V (point A in Figure 5a) and at 0.31 V (point B), respectively. These could likely correspond to one-electron oxidation of Cu(0) to Cu(I) and of Cu(I) to Cu(II). The possible reactions at Point A could be:



On the other hand, the following reactions might have happened at Point B:



For comparison with our Cu/LIC material, we also investigated the sensing behavior of pristine LIG electrodes. Figure 5b illustrates the CV curves of both Cu/LIC and LIG electrodes with and without the presence of H_2O_2 . The addition of H_2O_2 did not change the CV curve of the LIG electrode, representing no detection. In contrast, a drop in the oxidation peak at 0.31 V was observed with the exposure to 1 mM H_2O_2 in the case of the Cu/LIC electrode, demonstrating successful detection of H_2O_2 . The decreased oxidation current for the Cu/LIC electrode at 0.31 V could be attributed to the conversion of Cu(II) to Cu(I) by the simultaneous reduction of H_2O_2 . Such behavior was also reported in several other articles dealing with Cu/carbon-based biosensors [60–62]. The electrochemical reduction of H_2O_2 by Cu(II) occurred in two steps when H_2O_2 was applied to the electrolyte: (i) electrochemical reduction of Cu(II) to Cu(I) and (ii) electron transmission and O_2 generation, reducing the H_2O_2 into H_2O [63,64]. The following reactions could be attributed to the sensing mechanism:



The electron transfer behavior of the Cu/LIC electrode was investigated through cyclic voltammetry in a 0.02 M PBS electrolyte, varying the scan rate from 10 to 100 mV/s in the presence of 0.1 mM H_2O_2 (Figure 5c). As the scan rate increased, both the anodic (I_{pc}) and cathodic (I_{pa}) current peaks exhibited an augmentation, resulting in a concurrent increase

in I_{pa} and I_{pc} . This trend indicated that the scan rate was directly proportional to the peak current. Furthermore, an increase in the peak separation potential between the cathodic and anodic current peak potentials was observed with rising scan rates. This shift could be due to the reduction peaks shifting towards lower potential and oxidation peaks towards higher potential, confirming a quasi-reversible process at the Cu/LIC electrode surface, as depicted in Figure 5c. The relationship between redox peak currents and the square root of scan rate values is depicted in Figure 5d. The graph exhibited a linear correlation of I_{pa} and I_{pc} with the square root of the scan rate (v), expressed by the equations below:

$$I_{pa} = -100.4 + 91.6vs. \quad (R^2 = 0.98)$$

$$I_{pc} = 48.7 - 99.3vs. \quad (R^2 = 0.99)$$

where the high correlation coefficient R^2 values of 0.98 and 0.99 for the linear variations of I_{pa} and I_{pc} with v suggest that the electrochemical process followed a diffusion-assisted electron transfer mechanism, instead of a surface-controlled one [65].

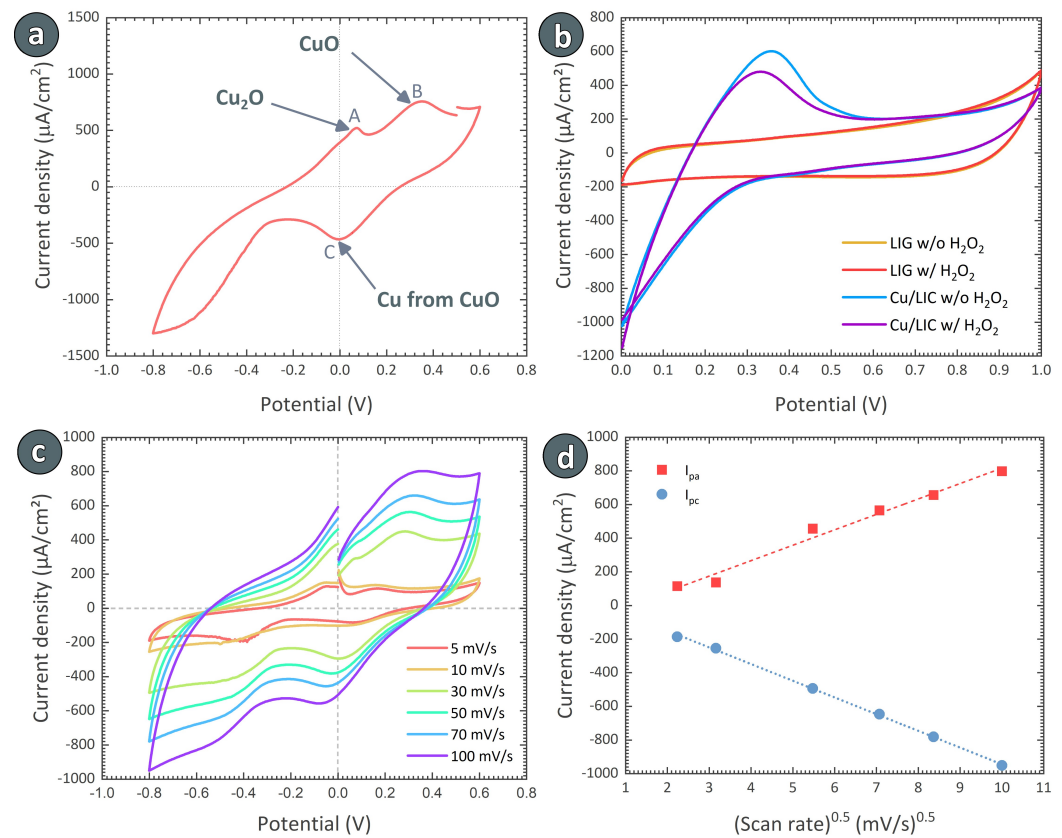


Figure 5. (a) CV of the Cu/LIC sample used to study the electrochemical sensing of H₂O₂, (b) CV of Cu/LIC and LIG in the absence and presence of 1 mM H₂O₂. (c) CV of Cu/LIC electrode at different scan rates in the presence of 1 mM H₂O₂. (d) Peak current of the CV curves with respect to the squared root of the scan rate for Cu/LIC electrode.

We further characterized the response (R_s) of our Cu/LIC electrode to H₂O₂ by the ratio of I_{pa} in CV without and with the presence of H₂O₂. Figure 6 plots the response values of Cu/LIC material for different concentrations of H₂O₂. Fitting the data points with nonlinear regression ($R^2 = 0.81$) revealed that the electrode material exhibited two sensing windows, 0.01 mM to 0.1 mM and 0.1 mM to 10 mM. We fitted the data points within each concentration window with linear correlations, as presented in the inset of Figure 6. The slope of the linear curve represents the sensitivity of the sensor material within each concentration window. The slope obtained for the concentration window 0.01 mM to 0.1 mM depicted a sensitivity of 2.65 mM⁻¹ with a limit of detection of 0.02 mM⁻¹.

The sensitivity within 0.1 mM to 10 mM was 0.01 mM^{-1} , exhibiting a limit of detection of 2.70 mM^{-1} .

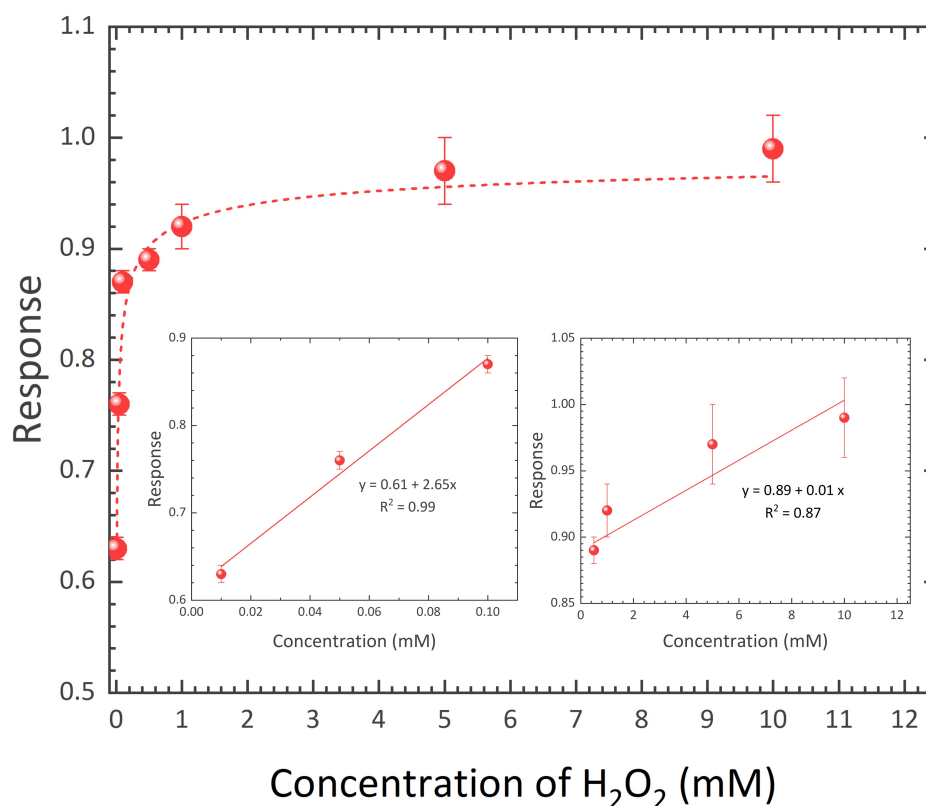


Figure 6. Response of the Cu/LIC electrode material for different concentrations of H₂O₂. Insets show the linear correlation between response and H₂O₂ concentration at two different ranges, left for 0.01 mM to 0.1 M and the right one for 0.1 mM to 10 mM.

We further compared the performance of our Cu/LIC electrode materials with other Cu/carbon composite electrodes for non-enzymatic H₂O₂ sensing. The performance of our electrode material is comparable to previously reported Cu/carbon-based electrode materials, as presented in Table 1. However, it should be noted that most of the reported materials used carbon nanotubes (CNTs) or graphene-based materials as the carbon counterpart. Processing these carbon materials is already complex and often requires expensive and time-consuming methodologies. Incorporating copper counterpart to these carbon nanomaterials further adds complexity to the entire process. In comparison, our synthesis process involving anodic electrodeposition and subsequent laser carbonization offers a simple and significantly rapid solution. Furthermore, even though we here only focused on copper-based anodic chitosan electrodeposition, other metals could potentially also be incorporated within chitosan hydrogel due to the ability of chitosan to form coordination bonds with other metals, such as iron, zinc, and chromium [66,67]. Laser carbonization of a chitosan complex with these metals could yield innovative nanocomposite materials for improved sensor applications. However, detailed experiments starting from the anodic electrodeposition and subsequent laser carbonization are needed to fully explore the potential of the presented methodology.

Table 1. Comparison of the performance of Cu/LIC with other published copper/carbon nanocomposite-based H₂O₂ sensors.

Materials	Synthesis Method	Linear Range	Sensitivity	Reference
Cu/carbon black	Physical mixing	0.003–2.338 mM	3.91 $\mu\text{A}\cdot\text{cm}^{-2}\cdot\text{mM}^{-1}$	[68]
Cu/MWCNT ¹	Chemical reduction	0.5–10,000 $\mu\text{M}/\text{L}$	0.37 $\mu\text{A}\cdot\text{L}\cdot\mu\text{M}^{-1}$	[69]
N-doped Carbon/Cu	Calcination	0.1–0.9 mM	1.27 $\text{mA}\cdot\text{mM}^{-1}$	[70]
Cu-rGO ²	Electrodeposition	0.1–18 mM	119.75 $\mu\text{A}\cdot\text{mM}^{-1}$	[71]
Cu-rGO	Electrochemical reduction	0.01–1 mM	20 $\mu\text{A}\cdot\text{cm}^{-2}\cdot\text{mM}^{-1}$	[72]
Cu-Graphene	Spray pyrolysis	32–803 $\mu\text{M}/\text{L}$	370 $\mu\text{A}\cdot\text{L}\cdot\text{cm}^{-2}\cdot\text{mM}^{-1}$	[44]
Cu/carbon	Anodic electrodeposition and pyrolysis	0.1–3 mM	58.9 $\mu\text{A}\cdot\text{cm}^{-2}\cdot\text{mM}^{-1}$	[13]
Cu/LIC	Anodic electrodeposition and laser carbonization	0.01–1 mM	2.65 mM^{-1}	This work

¹ MWCNT: Multiwall carbon nanotube. ² rGO: Reduced graphene oxide.

4. Conclusions

To summarize, this work presented a simple, straightforward, and rapid method for synthesizing Cu/carbon nanocomposite material through anodic electrodeposition of chitosan on a copper anode to yield a copper-coordinated chitosan hydrogel, followed by laser-induced carbonization of the composite. The optimization of the laser parameters required for the laser carbonization depicted that laser carbonization only happened within a narrow laser power range. Nevertheless, the laser treatment resulted in a transformation of chitosan precursor to a highly graphitic and porous carbon matrix. Even though the uniform distribution of copper was confirmed by elemental mapping, no crystalline phase of copper was detected within the nanocomposite, which could be attributed to the spontaneous nature of the laser carbonization. Even though a few crystalline copper particles were detected during transmission electron microscopy, the copper predominantly seemed to be in an amorphous state within the composite. Furthermore, a significant amount of NaCl was present within the Cu/LIC matrix, due to the use of NaOH and HCl during the electrodeposition process. A sensor electrode was further fabricated by combining the Cu/LIC material with LIG material on a polyimide substrate. The Cu/LIC composite demonstrated commendable non-enzymatic electrochemical sensing capabilities for H₂O₂, outperforming pristine LIG electrodes in PBS electrolyte. The composite exhibited a sensitivity of 2.65 mM^{-1} for concentrations ranging from 0.01 mM to 0.1 mM H₂O₂. The sensing performance of the Cu/LIC electrode was comparable to the previously reported Cu/carbon-based nanocomposite electrodes. Notably, our electrode-fabrication method highlights its facile and rapid nature, seemingly advantageous in comparison to the reported electrodes. Furthermore, future investigation could explore other metal/carbon composites, including iron, nickel, zinc, and chromium, promising to develop innovative and improved electrodes for diverse applications.

Author Contributions: Initiation and conceptualization, M.I. and J.G.K.; methodology, U.Z. and M.I.; validation, U.Z., V.B. and M.I.; formal analysis, U.Z., V.B. and M.I.; investigation, U.Z., P.K.R., V.B. and M.I.; resources, A.G., V.B. and J.G.K.; data curation, U.Z. and M.I.; writing—original draft preparation, U.Z., P.K.R., V.B. and M.I.; writing—review and editing, A.K., V.B., J.G.K. and M.I.; visualization, U.Z., P.K.R. and M.I.; supervision, A.G., V.B., J.G.K. and M.I.; project administration, V.B. and M.I.; funding acquisition, V.B. and J.G.K. All authors have read and agreed to the published version of the manuscript.

Funding: This research was funded by the Deutsche Forschungsgemeinschaft (DFG, German Research Foundation) under Germany's Excellence Strategy via the Excellence Cluster 3D Matter Made to Order (EXC-2082/1–390761711).

Data Availability Statement: The data presented in this study are available on request from the corresponding author due to legal/ethical reasons.

Acknowledgments: U.Z., M.I. and J.G.K. acknowledge support from the Deutsche Forschungsgemeinschaft (DFG, German Research Foundation) under Germany's Excellence Strategy via the Excellence Cluster 3D Matter Made to Order (EXC-2082/1–390761711). The authors also acknowledge Bastian E. Rapp and Anna Fischer from the University of Freiburg in Germany for their help with the transmission electron microscopy analysis. The authors thank Stefan Heissler and Peter Weidler of the Institute of Functional Interfaces of KIT for helping with Raman spectroscopy and X-ray diffraction, respectively.

Conflicts of Interest: The authors declare no conflicts of interest.

References

1. Shirvanimoghaddam, K.; Hamim, S.U.; Akbari, M.K.; Fakhrhoseini, S.M.; Khayyam, H.; Pakseresht, A.H.; Ghasali, E.; Zabet, M.; Munir, K.S.; Jia, S.; et al. Carbon fiber reinforced metal matrix composites: Fabrication processes and properties. *Compos. Part A Appl. Sci. Manuf.* **2017**, *92*, 70–96. [[CrossRef](#)]
2. Fritea, L.; Banica, F.; Costea, T.O.; Moldovan, L.; Dobjanschi, L.; Muresan, M.; Cavalu, S. Metal nanoparticles and carbon-based nanomaterials for improved performances of electrochemical (Bio) sensors with biomedical applications. *Materials* **2021**, *14*, 6319. [[CrossRef](#)] [[PubMed](#)]
3. Schultes, G.; Schmid-Engel, H.; Schwebke, S.; Werner, U. Granular metal–carbon nanocomposites as piezoresistive sensor films—Part 1: Experimental results and morphology. *J. Sens. Sens. Syst.* **2018**, *7*, 1–11. [[CrossRef](#)]
4. Zhou, S.; Zhou, J.; Pan, Y.; Wu, Q.; Ping, J. Wearable electrochemical sensors for plant small-molecule detection. *Trends Plant Sci.* **2024**, *29*, 219–231. [[CrossRef](#)] [[PubMed](#)]
5. Ta, Q.T.H.; Tran, N.M.; Tri, N.N.; Sreedhar, A.; Noh, J.S. Highly surface-active Si-doped TiO₂/Ti₃C₂T_x heterostructure for gas sensing and photodegradation of toxic matters. *Chem. Eng. J.* **2021**, *425*, 131437. [[CrossRef](#)]
6. Yu, R.; Chen, L.; Liu, Q.; Lin, J.; Tan, K.L.; Ng, S.C.; Chan, H.S.; Xu, G.Q.; Hor, T.A. Platinum deposition on carbon nanotubes via chemical modification. *Chem. Mater.* **1998**, *10*, 718–722. [[CrossRef](#)]
7. Tessonnier, J.P.; Ersen, O.; Weinberg, G.; Pham-Huu, C.; Su, D.S.; Schlogl, R. Selective deposition of metal nanoparticles inside or outside multiwalled carbon nanotubes. *ACS Nano* **2009**, *3*, 2081–2089. [[CrossRef](#)] [[PubMed](#)]
8. Mamleyev, E.R.; Falk, F.; Weidler, P.G.; Heissler, S.; Wadhwa, S.; Nassar, O.; Shyam Kumar, C.; Kübel, C.; Wöll, C.; Islam, M.; et al. Polyaramid-based flexible antibacterial coatings fabricated using laser-induced carbonization and copper electroplating. *ACS Appl. Mater. Interfaces* **2020**, *12*, 53193–53205. [[CrossRef](#)]
9. Chauhan, G.; Ángeles, A.L.; Gonzalez-González, E.; Kulkarni, M.M.; Cardenas-Benitez, B.; Jiménez, M.F.; Trujillo-de Santiago, G.; Alvarez, M.M.; Madou, M.; Martinez-Chapa, S.O. Nano-spaced Gold on Glassy Carbon Substrate for Controlling Cell Behavior. *Adv. Mater. Interfaces* **2020**, *7*, 2000238. [[CrossRef](#)]
10. Islam, M.; Dolle, C.; Sadaf, A.; Weidler, P.G.; Sharma, B.; Eggeler, Y.M.; Mager, D.; Korvink, J.G. Electrospun carbon nanofibre-assisted patterning of metal oxide nanostructures. *Microsyst. Nanoeng.* **2022**, *8*, 71. [[CrossRef](#)]
11. Mondal, K.; Ali, M.A.; Singh, C.; Sumana, G.; Malhotra, B.D.; Sharma, A. Highly sensitive porous carbon and metal/carbon conducting nanofiber based enzymatic biosensors for triglyceride detection. *Sens. Actuators B Chem.* **2017**, *246*, 202–214. [[CrossRef](#)]
12. Islam, M.; Keck, D.; Martinez-Duarte, R. Architected tungsten carbide electrodes using origami techniques. *Adv. Eng. Mater.* **2019**, *21*, 1900290. [[CrossRef](#)]
13. Islam, M.; Arya, N.; Weidler, P.; Korvink, J.; Badilita, V. Electrodeposition of chitosan enables synthesis of copper/carbon composites for H₂O₂ sensing. *Mater. Today Chem.* **2020**, *17*, 100338. [[CrossRef](#)]
14. Rai, P.K.; Gupta, A. Development of durable anticorrosion superhydrophobic electroformed copper tubular structures. *J. Manuf. Process.* **2023**, *85*, 236–245. [[CrossRef](#)]
15. Helú, M.A.B.; Liu, L. Rational shaping of hydrogel by electrodeposition under fluid mechanics for electrochemical writing on complex shaped surfaces at microscale. *Chem. Eng. J.* **2021**, *416*, 129029. [[CrossRef](#)]
16. Walsh, F.C.; Wang, S.; Zhou, N. The electrodeposition of composite coatings: Diversity, applications and challenges. *Curr. Opin. Electrochem.* **2020**, *20*, 8–19. [[CrossRef](#)]
17. Avcu, E.; Baştan, F.E.; Abdullah, H.Z.; Rehman, M.A.U.; Avcu, Y.Y.; Boccaccini, A.R. Electrophoretic deposition of chitosan-based composite coatings for biomedical applications: A review. *Prog. Mater. Sci.* **2019**, *103*, 69–108. [[CrossRef](#)]
18. Fusco, S.; Chatzipirpiridis, G.; Sivaraman, K.M.; Ergeneman, O.; Nelson, B.J.; Pané, S. Chitosan electrodeposition for microrobotic drug delivery. *Adv. Healthc. Mater.* **2013**, *2*, 1037–1044. [[CrossRef](#)]
19. Li, B.; Cheng, Y.; Dong, L.; Wang, Y.; Chen, J.; Huang, C.; Wei, D.; Feng, Y.; Jia, D.; Zhou, Y. Nitrogen doped and hierarchically porous carbons derived from chitosan hydrogel via rapid microwave carbonization for high-performance supercapacitors. *Carbon* **2017**, *122*, 592–603. [[CrossRef](#)]
20. Ababneh, H.; Hameed, B. Chitosan-derived hydrothermally carbonized materials and its applications: A review of recent literature. *Int. J. Biol. Macromol.* **2021**, *186*, 314–327. [[CrossRef](#)]
21. Tian, Y.; Estevez, D.; Wei, H.; Peng, M.; Zhou, L.; Xu, P.; Wu, C.; Yan, M.; Wang, H.; Peng, H.X.; et al. Chitosan-derived carbon aerogels with multiscale features for efficient microwave absorption. *Chem. Eng. J.* **2021**, *421*, 129781. [[CrossRef](#)]

22. Shi, N.; Liu, Q.; He, X.; Wang, G.; Chen, N.; Peng, J.; Ma, L. Molecular structure and formation mechanism of hydrochar from hydrothermal carbonization of carbohydrates. *Energy Fuels* **2019**, *33*, 9904–9915. [[CrossRef](#)]
23. Shen, Y. A review on hydrothermal carbonization of biomass and plastic wastes to energy products. *Biomass Bioenergy* **2020**, *134*, 105479. [[CrossRef](#)]
24. Ye, R.; James, D.K.; Tour, J.M. Laser-induced graphene. *Accounts Chem. Res.* **2018**, *51*, 1609–1620. [[CrossRef](#)] [[PubMed](#)]
25. Wang, H.; Zhao, Z.; Liu, P.; Guo, X. Laser-induced graphene based flexible electronic devices. *Biosensors* **2022**, *12*, 55. [[CrossRef](#)] [[PubMed](#)]
26. Ye, R.; James, D.K.; Tour, J.M. Laser-induced graphene: From discovery to translation. *Adv. Mater.* **2019**, *31*, 1803621. [[CrossRef](#)] [[PubMed](#)]
27. Kaur, S.; Mager, D.; Korvink, J.G.; Islam, M. Unraveling the dependency on multiple passes in laser-induced graphene electrodes for supercapacitor and H₂O₂ sensing. *Mater. Sci. Energy Technol.* **2021**, *4*, 407–412. [[CrossRef](#)]
28. Chyan, Y.; Ye, R.; Li, Y.; Singh, S.P.; Arnusch, C.J.; Tour, J.M. Laser-induced graphene by multiple lasing: Toward electronics on cloth, paper, and food. *ACS Nano* **2018**, *12*, 2176–2183. [[CrossRef](#)]
29. Mamleyev, E.R.; Weidler, P.G.; Nefedov, A.; Szabó, D.V.; Islam, M.; Mager, D.; Korvink, J.G. Nano-and microstructured copper/copper oxide composites on laser-induced carbon for enzyme-free glucose sensors. *ACS Appl. Nano Mater.* **2021**, *4*, 13747–13760. [[CrossRef](#)]
30. Bachmann, A.L.; Ferris, A.L.; Im, S.; Dickey, M.D.; Lazarus, N. Laser-Induced Graphene from SU-8 Photoresist: Toward Functional Micromolding. *ACS Appl. Eng. Mater.* **2022**, *1*, 222–228. [[CrossRef](#)]
31. Wan, Z.; Nguyen, N.T.; Gao, Y.; Li, Q. Laser induced graphene for biosensors. *Sustain. Mater. Technol.* **2020**, *25*, e00205. [[CrossRef](#)]
32. Liu, J.; Ji, H.; Lv, X.; Zeng, C.; Li, H.; Li, F.; Qu, B.; Cui, F.; Zhou, Q. Laser-induced graphene (LIG)-driven medical sensors for health monitoring and diseases diagnosis. *Microchim. Acta* **2022**, *189*, 54. [[CrossRef](#)] [[PubMed](#)]
33. Wanjari, V.P.; Reddy, A.S.; Duttagupta, S.P.; Singh, S.P. Laser-induced graphene-based electrochemical biosensors for environmental applications: A perspective. *Environ. Sci. Pollut. Res.* **2023**, *30*, 42643–42657. [[CrossRef](#)] [[PubMed](#)]
34. Zhu, J.; Huang, X.; Song, W. Physical and chemical sensors on the basis of laser-induced graphene: mechanisms, applications, and perspectives. *ACS Nano* **2021**, *15*, 18708–18741. [[CrossRef](#)] [[PubMed](#)]
35. Mamleyev, E.R.; Heissler, S.; Nefedov, A.; Weidler, P.G.; Nordin, N.; Kudryashov, V.V.; Länge, K.; MacKinnon, N.; Sharma, S. Laser-induced hierarchical carbon patterns on polyimide substrates for flexible urea sensors. *NPJ Flex. Electron.* **2019**, *3*, 2. [[CrossRef](#)]
36. Xu, G.; Jarjes, Z.A.; Desprez, V.; Kilmartin, P.A.; Travas-Sejdic, J. Sensitive, selective, disposable electrochemical dopamine sensor based on PEDOT-modified laser scribed graphene. *Biosens. Bioelectron.* **2018**, *107*, 184–191. [[CrossRef](#)] [[PubMed](#)]
37. Zhang, Y.; Zhu, H.; Sun, P.; Sun, C.K.; Huang, H.; Guan, S.; Liu, H.; Zhang, H.; Zhang, C.; Qin, K.R. Laser-induced graphene-based non-enzymatic sensor for detection of hydrogen peroxide. *Electroanalysis* **2019**, *31*, 1334–1341. [[CrossRef](#)]
38. Matias, T.A.; de Faria, L.V.; Rocha, R.G.; Silva, M.N.; Nossol, E.; Richter, E.M.; Muñoz, R.A. Prussian blue-modified laser-induced graphene platforms for detection of hydrogen peroxide. *Microchim. Acta* **2022**, *189*, 188. [[CrossRef](#)]
39. Fenzl, C.; Nayak, P.; Hirsch, T.; Wolfbeis, O.S.; Alshareef, H.N.; Baeumner, A.J. Laser-scribed graphene electrodes for aptamer-based biosensing. *ACS Sens.* **2017**, *2*, 616–620. [[CrossRef](#)]
40. Zhu, J.; Liu, S.; Hu, Z.; Zhang, X.; Yi, N.; Tang, K.; Dexheimer, M.G.; Lian, X.; Wang, Q.; Yang, J.; et al. Laser-induced graphene non-enzymatic glucose sensors for on-body measurements. *Biosens. Bioelectron.* **2021**, *193*, 113606. [[CrossRef](#)]
41. Yu, S.; Cui, J.; Wang, J.; Zhong, C.; Wang, X.; Wang, N. Facile fabrication of Cu (II) coordinated chitosan-based magnetic material for effective adsorption of reactive brilliant red from aqueous solution. *Int. J. Biol. Macromol.* **2020**, *149*, 562–571. [[CrossRef](#)] [[PubMed](#)]
42. Xiao, Y.; Shen, G.; Zheng, W.; Fu, J.; Fu, F.; Hu, X.; Jin, Z.; Liu, X. Remarkable durability of the antibacterial function achieved via a coordination effect of Cu (II) ion and chitosan grafted on cotton fibers. *Cellulose* **2022**, *29*, 1003–1015. [[CrossRef](#)]
43. Deng, Z.; Li, L.; Ren, Y.; Ma, C.; Liang, J.; Dong, K.; Liu, Q.; Luo, Y.; Li, T.; Tang, B.; et al. Highly efficient two-electron electroreduction of oxygen into hydrogen peroxide over Cu-doped TiO₂. *Nano Res.* **2022**, *15*, 3880–3885. [[CrossRef](#)]
44. Alencar, L.M.; Silva, A.W.; Trindade, M.A.; Salvatierra, R.V.; Martins, C.A.; Souza, V.H. One-step synthesis of crumpled graphene fully decorated by copper-based nanoparticles: Application in H₂O₂ sensing. *Sens. Actuators B Chem.* **2022**, *360*, 131649. [[CrossRef](#)]
45. Yuan, K.; Zhang, Y.; Huang, S.; Yang, S.; Zhao, S.; Liu, F.; Peng, Q.; Zhao, Y.; Zhang, G.; Fan, J.; et al. Copper nanoflowers on carbon cloth as a flexible electrode toward both enzymeless electrocatalytic glucose and H₂O₂. *Electroanalysis* **2021**, *33*, 1800–1809. [[CrossRef](#)]
46. Shaner, S.W.; Islam, M.; Kristoffersen, M.B.; Azmi, R.; Heissler, S.; Ortiz-Catalan, M.; Korvink, J.G.; Asplund, M. Skin stimulation and recording: Moving towards metal-free electrodes. *Biosens. Bioelectron. X* **2022**, *11*, 100143. [[CrossRef](#)]
47. Cañado, L.; Takai, K.; Enoki, T.; Endo, M.; Kim, Y.; Mizusaki, H.; Jorio, A.; Coelho, L.; Magalhães-Paniago, R.; Pimenta, M. General equation for the determination of the crystallite size L_a of nanographite by Raman spectroscopy. *Appl. Phys. Lett.* **2006**, *88*, 163106. [[CrossRef](#)]
48. Kulyk, B.; Silva, B.F.; Carvalho, A.F.; Silvestre, S.; Fernandes, A.J.; Martins, R.; Fortunato, E.; Costa, F.M. Laser-induced graphene from paper for mechanical sensing. *ACS Appl. Mater. Interfaces* **2021**, *13*, 10210–10221. [[CrossRef](#)]
49. Huang, L.; Su, J.; Song, Y.; Ye, R. Laser-induced graphene: En route to smart sensing. *Nano-Micro Lett.* **2020**, *12*, 157. [[CrossRef](#)]

50. Barbhuiya, N.H.; Kumar, A.; Singh, S.P. A journey of laser-induced graphene in water treatment. *Trans. Indian Natl. Acad. Eng.* **2021**, *6*, 159–171. [[CrossRef](#)]
51. Abdou, S.M.; Moharam, H. Characterization of table salt samples from different origins and ESR detection of the induced effects due to gamma irradiation. *Proc. J. Phys. Conf. Ser.* **2019**, *1253*, 012036. [[CrossRef](#)]
52. Dabera, G.D.M.; Walker, M.; Sanchez, A.M.; Pereira, H.J.; Beanland, R.; Hatton, R.A. Retarding oxidation of copper nanoparticles without electrical isolation and the size dependence of work function. *Nat. Commun.* **2017**, *8*, 1894. [[CrossRef](#)] [[PubMed](#)]
53. Popok, V.N.; Novikov, S.M.; Lebedinskij, Y.Y.; Markeev, A.M.; Andreev, A.A.; Trunkin, I.N.; Arsenin, A.V.; Volkov, V.S. Gas-aggregated copper nanoparticles with long-term plasmon resonance stability. *Plasmonics* **2021**, *16*, 333–340. [[CrossRef](#)]
54. Dennison, J.R.; Holtz, M.; Swain, G. Raman spectroscopy of carbon materials. *Spectroscopy* **1996**, *11*, 38–45.
55. Dresselhaus, M.; Jorio, A.; Saito, R. Characterizing graphene, graphite, and carbon nanotubes by Raman spectroscopy. *Annu. Rev. Condens. Matter Phys.* **2010**, *1*, 89–108. [[CrossRef](#)]
56. Ribeiro-Soares, J.; Oliveros, M.; Garin, C.; David, M.; Martins, L.; Almeida, C.; Martins-Ferreira, E.; Takai, K.; Enoki, T.; Magalhães-Paniago, R.; et al. Structural analysis of polycrystalline graphene systems by Raman spectroscopy. *Carbon* **2015**, *95*, 646–652. [[CrossRef](#)]
57. Pillet, G.; Sapelkin, A.; Bacs, W.; Monthieux, M.; Puech, P. Size-controlled graphene-based materials prepared by annealing of pitch-based cokes: G band phonon line broadening effects due to high pressure, crystallite size, and merging with D' band. *J. Raman Spectrosc.* **2019**, *50*, 1861–1866. [[CrossRef](#)]
58. Beyssac, O.; Lazzeri, M. Application of Raman spectroscopy to the study of graphitic carbons in the Earth Sciences. *Eur. Mineral. Union Notes Mineral.* **2012**, *12*, 415–454.
59. Sole, C.; Drewett, N.E.; Hardwick, L.J. In situ Raman study of lithium-ion intercalation into microcrystalline graphite. *Faraday Discuss.* **2014**, *172*, 223–237. [[CrossRef](#)]
60. Tian, W.; Ding, X.; Jiang, F.; Du, X.; Shi, J.; Zhang, J. Green Preparation of Cu Nanoparticles via Gallic Acid Applied to H₂O₂ Detection. *J. Electron. Mater.* **2022**, *51*, 1752–1758. [[CrossRef](#)]
61. Ammara, S.; Shamailla, S.; Bokhari, A.; Sabah, A. Nonenzymatic glucose sensor with high performance electrodeposited nickel/copper/carbon nanotubes nanocomposite electrode. *J. Phys. Chem. Solids* **2018**, *120*, 12–19. [[CrossRef](#)]
62. Xie, L.; Asiri, A.M.; Sun, X. Monolithically integrated copper phosphide nanowire: An efficient electrocatalyst for sensitive and selective nonenzymatic glucose detection. *Sens. Actuators B Chem.* **2017**, *244*, 11–16. [[CrossRef](#)]
63. Lee, W.C.; Kim, K.B.; Gurudatt, N.; Hussain, K.K.; Choi, C.S.; Park, D.S.; Shim, Y.B. Comparison of enzymatic and non-enzymatic glucose sensors based on hierarchical Au-Ni alloy with conductive polymer. *Biosens. Bioelectron.* **2019**, *130*, 48–54. [[CrossRef](#)] [[PubMed](#)]
64. Yang, Z.; Tan, X.; Tang, D.; Li, J.; Ma, J. A tale of two metal ions: Contrasting behaviors of high oxidation states of Cu and Mn in a bicarbonate–H₂O₂ system. *Environ. Sci. Water Res. Technol.* **2021**, *7*, 479–486. [[CrossRef](#)]
65. Alegret, S.; Merkoçi, A. *Electrochemical Sensor Analysis*; Elsevier: Amsterdam, The Netherlands, 2007.
66. Molnár, Á. The use of chitosan-based metal catalysts in organic transformations. *Coord. Chem. Rev.* **2019**, *388*, 126–171. [[CrossRef](#)]
67. Varma, A.; Deshpande, S.; Kennedy, J. Metal complexation by chitosan and its derivatives: A review. *Carbohydr. Polym.* **2004**, *55*, 77–93. [[CrossRef](#)]
68. Mei, L.; Zhang, P.; Chen, J.; Chen, D.; Quan, Y.; Gu, N.; Zhang, G.; Cui, R. Non-enzymatic sensing of glucose and hydrogen peroxide using a glassy carbon electrode modified with a nanocomposite consisting of nanoporous copper, carbon black and nafion. *Microchim. Acta* **2016**, *183*, 1359–1365. [[CrossRef](#)]
69. Rezaei, B.; Askarpour, N.; Ghiaci, M.; Niyazian, F.; Ensafi, A. Synthesis of functionalized MWCNTs decorated with copper nanoparticles and its application as a sensitive sensor for amperometric detection of H₂O₂. *Electroanalysis* **2015**, *27*, 1457–1465. [[CrossRef](#)]
70. Wei, C.; Liu, Y.; Li, X.; Zhao, J.; Ren, Z.; Pang, H. Nitrogen-Doped Carbon–Copper Nanohybrids as Electrocatalysts in H₂O₂ and Glucose Sensing. *ChemElectroChem* **2014**, *1*, 799–807. [[CrossRef](#)]
71. Nia, P.M.; Woi, P.M.; Alias, Y. Facile one-step electrochemical deposition of copper nanoparticles and reduced graphene oxide as nonenzymatic hydrogen peroxide sensor. *Appl. Surf. Sci.* **2017**, *413*, 56–65.
72. Temur, E.; Eryiğit, M.; Urhan, B.K.; Demir, Ü.; Özer, T.Ö. Cu/Electrochemically reduced graphene oxide layered nanocomposite for non-enzymatic H₂O₂ sensor. *Mater. Today Proc.* **2021**, *46*, 6971–6975. [[CrossRef](#)]

Disclaimer/Publisher's Note: The statements, opinions and data contained in all publications are solely those of the individual author(s) and contributor(s) and not of MDPI and/or the editor(s). MDPI and/or the editor(s) disclaim responsibility for any injury to people or property resulting from any ideas, methods, instructions or products referred to in the content.